Opto-Electronic Advances

Original Article

2020, Vol. 3, No. 12

DOI: 10.29026/oea.2020.200028

Athermal third harmonic generation in micro-ring resonators

Shaohao Wang[1,6]*, Yuhua Li[2,7], Brent E. Little[3], Leiran Wang[3,4], Xiang Wang[5], Roy R. Davidson[5] and Sai Tak Chu[2]*

Nonlinear high-harmonic generation in micro-resonators is a common technique used to extend the operating range of applications such as self-referencing systems and coherent communications in the visible region. However, the generated high-harmonic emissions are subject to a resonance shift with a change in temperature. We present a comprehensive study of the thermal behavior induced phase mismatch that shows this resonance shift can be compensated by a combination of the linear and nonlinear thermo-optics effects. Using this model, we predict and experimentally demonstrate visible third harmonic modes having temperature dependent wavelength shifts between −2.84 pm/ºC and 2.35 pm/ºC when pumped at the L-band. Besides providing a new way to achieve athermal operation, this also allows one to measure the thermal coefficients and Q-factor of the visible modes. Through steady state analysis, we have also identified the existence of stable athermal third harmonic generation and experimentally demonstrated orthogonally pumped visible third harmonic modes with a temperature dependent wavelength shift of 0.05 pm/ºC over a temperature range of 12 ºC. Our findings promise a configurable and active temperature dependent wavelength shift compensation scheme for highly efficient and precise visible emission generation for potential 2*f*–3*f* self-referencing in metrology, biological and chemical sensing applications.

Keywords: third-harmonic generation; thermodynamics; micro-resonators

Wang S H, Li Y H, Little B E, Wang L R, Wang X et al. Athermal third harmonic generation in micro-ring resonators. *Opto-Electron Adv* **3**, 200028 (2020).

Introduction

Nonlinear high-harmonic generation in micro-resonators using a pump at telecom wavelengths is a popular technique used to extend the operating range of applicationfs such as *f*–2*f* and 2*f*–3*f* self-referencing systems and coherent communications in the visible region[1–16]. Recent demonstration of visible emission generation in microring resonators (MRRs) via third-harmonic generation (THG) in a number of nonlinear integrated optical circuit platforms, such as silicon nitride[7–9], composite AlN/Si_3N_4[10–11], lithium niobite (LN) on insulator[12], and highly doped silica glass (HDSG)[13], promises the potential of on-chip integration of a visible reference source in the advanced integrated circuits using these platforms. This is especially important in the development of compact and practical self-referencing and sensing systems.

The critical criteria for effective THG of visible emission in wavelength selective MRRs lies is the phase matching between the resonances of the pump mode and the third harmonic (TH) modes. Similar to that of the

[1]FZU-Jinjiang Joint Institute of Microelectronics, Jinjiang Science and Education Park, Fuzhou University, Jinjiang 362200, China. [2]Department of Physics, City University of Hong Kong, Kowloon Tong, Hong Kong 999077, China. [3]State Key Laboratory of Transient Optics and Photonics, Xi'an Institute of Optics and Precision Mechanics, Chinese Academy of Sciences, Xi'an 710119, China. [4]University of Chinese Academy of Sciences, Beijing 100049, China.[5]QXP Technology, Xi'an 710311, China. [6]Department of Microelectronics Science and Technology, Qi Shan Campus, Fuzhou University, Fuzhou 350108, China. [7]Key Laboratory of Optical Field Manipulation of Zhejiang Province, Department of Physics, Zhejiang Sci-Tech University, Hangzhou 310018, China.

*Correspondence: S H Wang, E-mail: shwang@fzu.edu.cn; S T Chu, E-mail: saitchu@cityu.edu.hk

Received: 7 July 2020; Accepted: 25 August 2020; Published: 24 December 2020

Kerr frequency comb generation[17–26], understanding and controlling the thermal behaviors of these modes remain a challenge in maximizing their THG efficiency[27], as both the linear and nonlinear thermo-optial (TO) effects impart refractive index variations of the waveguide[19–26,28–42]. For platforms with a positive linear TO coefficients, the linear TO effect gives rise of tens of pm/°C temperature dependent wavelength shifts (TDWS) to the cold-cavity resonances of MRRs[17–19]. It is possible to compensate the intrinsic linear TDWS by adding a cladding having a negative TO coefficient, such as polymer[31–36] or TiO_2[37–38] and liquid crystal[39] to offset the thermal dependency[30]. These types of structures can achieve nearly athermal operation over temperature ranges of tens of degrees. However, the THG process must also account for the nonlinear TO effects as the localized heat generated by the high intra-cavity pump power can also introduce a redshift to the resonance[18,28–29]. While this nonlinear TO effect can be compensated by the photorefractive effect in LN waveguide devices[23–24] or by changing the structure of MRRs[41] or by adopting the electrical or optical cooling approaches[26,42], these compensation methods are either unavailable or add complexity to the design in the complementary metal oxide semiconductor (CMOS) compatible MRRs devices.

Therefore, it is necessary to explore other approaches in the realization of temperature insensitive operation that will also address effects such as Kerr nonlinearity induced phase shift in the determination of the phase matching condition.

This work presents the development of a dynamic model to investigate the thermal dependency of the THG phase matching condition, which is affected by the linear and nonlinear TO effects induced phase mismatch. By using this model, we indirectly measure the thermal coefficients as well as Q-factor of the visible mode. We also perform the steady state analysis to investigate the TDWS of the TH modes as well as the existence of athermal THG operation on the thermal mismatch between the pump mode and the TH modes. We are able to verify the model's predictions experimentally in a series of silicon rich HDSG add-drop MRR filters. We further classify the different types of visible TH modes from their THG efficiencies as well as TDWS. By precisely pairing the pump and the TH modes at different thermal mismatches, it is now possible to configure effective TDWS of the TH modes for a given MRR leading to athermal THG at different wavelengths.

Principle and theory

Steady-state thermal dynamics model

In this work, we consider both linear and nonlinear TO effects of THG in MRRs. The discussion requires steady and uniform intra-cavity power distribution for both the pump and the TH waves, in which both optical power and net heat are assumed to be evenly distributed over the ring cavity, so that the averaged local thermal nonlinearity still correlates with the Kerr nonlinearity in the moving reference frame. Experimentally, this uniform intra-cavity power distribution is achieved by injecting continuous wave (CW) laser into the resonance with large normal dispersion. Different from generating Kerr frequency combs[17–18], the sweep speed of the pump wavelength has to be slow so that the cavity can be thermally self-stabilized.

When intra-cavity power of the pump I_p is much larger than I_t, the intra-cavity power of TH emission, it is reasonable to neglect the self-phase modulation (SPM), cross-phase modulation (XPM), and the pump depletion induced by the TH emission. By using the steady-state assumption for I_p and I_t, from the coupled thermal dynamics model for THG in MRRs (See Supplementary Discussion III), we have[13]

$$\left(-\mathrm{i}\Omega_p-\mathrm{i}\xi_p\omega_{p0}\delta T-\frac{\kappa_p}{2}\right)a_p -\mathrm{i}\left(\Theta_p+g_{pp}\right)I_p a_p-\mathrm{i}\sqrt{\kappa_{pe}}p_i=0 \quad , \tag{1}$$

$$\left(-\mathrm{i}\Omega_t-\mathrm{i}\xi_t\omega_{t0}\delta T-\frac{\kappa_t}{2}\right)a_t -\mathrm{i}\left(\Theta_t+g_{tp}\right)I_p a_t=\mathrm{i}g_{TH}\hbar\omega_p a_p^3 \quad , \tag{2}$$

where, $|a_p|^2 = I_p/\hbar\omega_p$ and $|a_t|^2 = I_t/3\hbar\omega_p$ corresponds to the photon numbers of the pump and TH emission, respectively, and ω_p is the angular frequency of input pump. $\Omega_p = \omega_p - \omega_{p0}$ and $\Omega_t = 3\omega_p - \omega_{t0}$ are the cold-cavity resonance detuning of the pump and TH wave, respectively, where ω_{p0} and ω_{t0} are the cold-cavity resonance frequencies of pump and TH modes at temperature T_0, respectively. Here, $\delta T = T - T_0$ is the difference between temperature T and T_0. ξ_p and ξ_t are the linear TO coefficients of the pump and TH modes, respectively[28], κ_p and κ_t are the overall losses of the pump and TH modes, respectively. Here, we define Θ_p and Θ_t as the nonlinear TO shift rate of the pump and the TH emission in rad/J, (See Supplementary Discussion III), respectively. g_{pp} is the nonlinear factors of the pump and g_{tp} is the XPM factors

of TH emission and g_{TH} is the growth rate of the THG. In Eq. (1), κ_{pe} is the external coupling rate of the pump and $|p_i|^2 = P_i/\hbar\omega_p$ refers to the photon number of P_i. In Eq. (2), XPM effect dominates the Kerr nonlinearity.

Tunable TO phase mismatch for THG in MRRs

The overall THG efficiency depends strongly on the phase matching condition between the pump and the TH modes. It is more convenient to express the phase matching condition in terms of the phase mismatch $\Delta\beta_{total}$ between these modes, which can be approximately expressed as

$$\Delta\beta_{total} \approx \frac{\Delta n_g}{c}\left[\Omega_t + \Omega_{TL}(\delta T) + \Omega_{TNL}(\Delta T) + \Omega_{KNL}\right] , \quad (3)$$

where, the terms $\Omega_{TL} = \xi_t\omega_{t0}\delta T$, $\Omega_{TNL} = \Theta_t I_p$, and $\Omega_{KNL} = g_{tp}I_p$ represent the linear TO phase mismatch, the nonlinear TO phase mismatch, and the Kerr nonlinear phase mismatch in THG, respectively. Here, Δn_g is the difference of group velocity and the c is the speed of light in vacuum. From Eq. (2), we can analytically write the dependence of I_t of the TH mode as

$$I_t = \frac{4}{3}\cdot\frac{g_{TH}^2 I_p^3}{\kappa_t^2 + 4\left[\Omega_t + \Omega_{TL} + \Omega_{TNL} + \Omega_{KNL}\right]^2} . \quad (4)$$

As shown in Eq. (4), the maximum efficiency occurs at its minimum mismatch. We also notice that, due to the nonlinear phase mismatches, the intensity of THG signal is proportional to the intra-cavity energy instead of the input pump power. Therefore, we should define $\eta = 4g_{TH}^2/(3\kappa_t^2)$ as the overall THG efficiency in J^{-2}. For HDSG MRRs, since the calculated Kerr nonlinear coefficient of the TH emission γ_{tt} =1.35 $W^{-1}\cdot m^{-1}$ @ 517 nm, we can neglect the Ω_{KNL} term with a factor $g_{tp} < 6.24\times10^7$ pJ^{-1} in Eq. (2) in the analysis which is two orders of magnitude smaller than Θ_t as shown in Table 1[43].

Figure 1(a) illustrates the individual contributions to the cavity resonance tuning due to the linear and nonlinear TO effects. It shows that while the Ω_{TNL} can only produce a redshift, Ω_{TL} can produce a red or blue shift depending on whether the temperature is ramped up or down[10,19–22]. From the nearly phase matching assumption, i.e. $\Delta\beta_{total} \approx 0$, we have $\Omega_{TL} + \Omega_{TNL} = \xi_t\omega_{t0}\delta T + \Theta_t I_p \approx -\Omega_t$ from Eq. (3) which implies a decrease of δT resulting in a negative Ω_{TL} that can be used to compensate the increase of Ω_{TNL}, as shown in Fig. 1(b). A better way to understand the interplay between the thermal behaviors of the pump and TH modes is to consider the thermal dynamic of

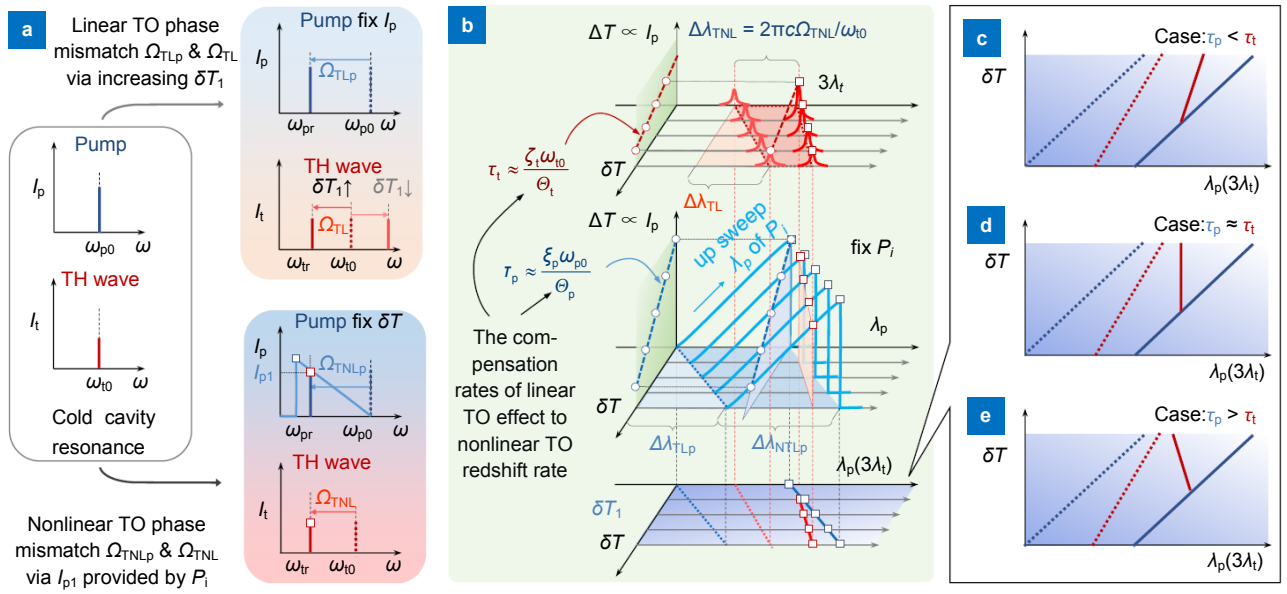

Fig. 1 | (**a**) The cavity resonance of MRRs can be linearly tuned by varying the chip temperature δT or nonlinearly tuned by controlling the intra-cavity pump energy I_p through nonlinear TO effects. (**b**) In the wavelength domain, when δT increases, the cold-cavity resonance wavelengths of the TH mode (in red dot line) and the pump mode (in blue dot line) will linearly redshift $\Delta\lambda_{TL}$ and $\Delta\lambda_{TLp}$, respectively. When up sweeping the CW input pump wavelength λ_p and δT are fixed, the corresponding I_p will induce nonlinear redshift $\Delta\lambda_{TNL}$ and $\Delta\lambda_{TNLp}$ to the resonance wavelengths of the TH and pump modes, respectively. For the pump mode, when λ_p is fixed, the trace of blue open circles determines τ_p which is the ratio between δT and I_p. Similarly, the trace of red open circles in the upper part of (b) gives the ratio τ_p. The overall effects of $\Delta\lambda_{TL}$ and $\Delta\lambda_{TNL}$ determine the effective TDWS of the TH mode which becomes a δT-λ_p relationship by mapping the trace of red open squares to the lower part of (b). For the pump mode, its TDWS is only related the linear TO redshift $\Delta\lambda_{TLp}$ whose trace was shown as blue open squares plotted in the δT-λ_p diagram. (**c – e**) The thermal mismatch between τ_p and τ_t will determine the effective TDWS of the TH mode, which leads to (c) a positive TDWS when $\tau_p < \tau_t$ and (d) a zero TDWS when $\tau_p \approx \tau_t$ and (e) a negative TDWS when $\tau_p > \tau_t$ in the δT-λ_p diagram.

these modes separately. We can denote $\tau_i = \xi_i\omega_{i0}/\Theta_i$, i = p, t, as the ratio between the linear TO compensation rates of decreasing δT and the nonlinear TO shift rate induced by I_p for the pump and TH modes, respectively, as the measure of the effective TDWS of the modes. It is now possible to map the δT–λ_p relationship and plot the TDWS of TH (red dot lines) and the pump mode (blue lines) separately as shown in Fig. 1(b), where λ_p is the pump wavelength to obtain the resulting effective TDWS of the TH mode (red solid lines).

Figures 1(c)–1(e) show three scenarios of the effective TDWS of the TH mode in the δT-λ_p diagrams at different values of τ_t. As long as the TH mode is thermally matched with the pump mode, i.e. the thermal mismatch $\Delta\tau = \tau_p - \tau_t \approx 0$, their resonances can be kept correlated while maintaining the necessary phase matching condition, without the need for any external compensation, as shown in Fig. 1(d). In contrast, the thermal mismatch between the pump and TH modes will cause misalignment between their resonances and affect the THG efficiency. Figures 1(c) and 1(e) show when it is under- and over-compensated, respectively.

The existence of stable athermal THG in MRRs

In MRRs, the dependence of I_p to the input pump power P_i and the pump detuning Ω_p is a nonlinear relationship instead of the linear one[44–45]. In the HDSG MRRs, the dominant nonlinear TO effect further reduces the nonlinear threshold by two orders of magnitude. In this case, only configuring a fixed $\Delta\tau$ may not keep the thermal matching condition over a broad range of temperature. From Eq. (2), the existence of stable athermal modes can be found by equating $\partial\Omega_t/\partial T = 0$. Applying this athermal condition into Eq. (1) leads to the following normalized equation which describes the dependence of Ω_p on P_i and I_p in nearly athermal THG via steady state analysis, (see Supplementary information Eq. S5.3).

$$F^2 = \left[1 + (\rho - \alpha)^2\right]\rho, \tag{5}$$

where, $\alpha = 2\Omega_p/\kappa_p$ is the normalized pump detuning which is proportional to Ω_p, $\rho = -2\Theta_p\Delta\tau\delta T/\kappa_p$ is the normalized intra-cavity pump power, and $F^2 = 8\Theta_p\kappa_{pe}\Delta\tau P_i/(\kappa_p^3\tau_t)$ is the normalized intra-cavity pump power.

In Eq. (5), only when $|\alpha| > \sqrt{3}$, can there be three equilibria for one value of F^2 [45], which is the criteria for the existence of stable athermal TH modes. Figure 2(a) plots the nonlinear relationship between α and ρ using Eq. (5) with different F^2, in which the real roots of α are plotted as dashed lines. In Fig. 2(a), the green and blue solid lines show that α remains constant within a certain temperature range of δT, which implies the existence of stable athermal TH modes built up by fixed input pump powers. Moreover, different from the case of Kerr nonlinearity[45], in athermal THG, the opposite sign of α implies that the dominating nonlinear TO effect can generate stable athermal modes on the blue edge of the pump resonance that are accessible by the sweeping of the pump signal.

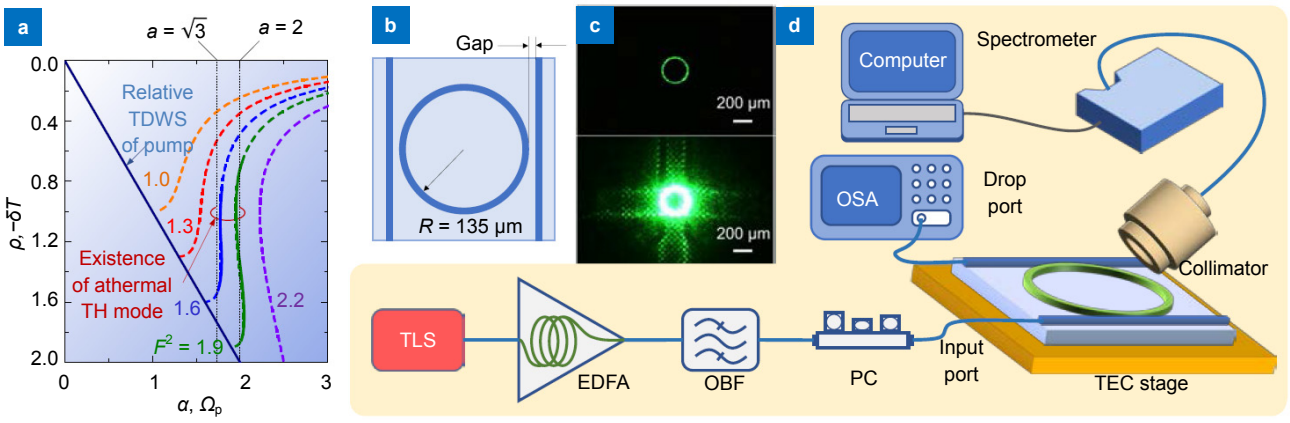

Fig. 2 | (**a**) The relationship between the normalized pump detuning α and the intra-cavity pump power ρ when the input pump power F^2 is fixed. The existence of stable athermal TH modes were shown in blue (F^2 = 1.6) and green (F^2 = 1.9) solid lines when $|\alpha| > \sqrt{3}$. (**b**) Four-port MRR add-drop filter schematic showing a variable bus-ring gap separation design. (**c**) The captured green side-emissions via THG in MRRs at different chip temperatures. (**d**) Schematic experimental setup of THG in MRR. TLS: tunable laser source; EDFA: erbium-doped fiber amplifier; OBF: optical bandpass filter; PC: polarization controller; TEC: thermoelectric cooler; OSA: optical spectrum analyzer.

MRR fabrication and experimental setup

A series of HDSG four-port single ring MRR add-drop filters are fabricated for the investigation in which a ring resonator with radius of R = 135 μm is side coupled to an input and output bus waveguide as shown in Fig. 2(b). The cross-section of both the rings and the bus waveguides are 2 μm × 1 μm, which consist of highly doped glass of refractive index 1.70 and cladded with silica. The Q-factors of the MRRs are varied by using a gap separation of 0.8 μm (R-1, R-3) and 1.0 μm (R-2), respectively. The corresponding transmission spectrum and the Q factors of the devices are shown in Figs. 1(a) and (b) as well as table 2 in ref.[13], respectively. The advantage of the device having a drop port is to allow the direct monitoring of $I_{\rm p}$. All the devices are pigtailed to fiber arrays where the coupling loss at the pump wavelength is between 0.75 and 1 dB/facet. It is important to note that the coupling coefficient between the ring and the bus is between 2% to 7% at the pump wavelength but there is virtually no coupling at the TH wavelength, as can be seen from the TH emission photos in Fig. 2(c), where only the ring is lit up during THG. Additional details on the fabrication of the MRR devices can be found in refs.[46–48].

The schematic of the experimental setup for monitoring the THG emission is shown in Fig. 2(d). A CW pump from the TLS, (Agilent 8164A) is amplified by an EDFA (Amonics, AEDFA-CL-30-R-FA). An OBF is used to reject the amplified spontaneous emission (ASE) of the amplified pump before it is launched into the input port of the MRR add-drop filter in the experiment. Since the THG emission cannot couple to the bus waveguide, it is necessary to collect the emission from the top of the ring by a collimator (Thorlabs F671SMA), then the collected signal is transmitted to the spectrometer (Ocean Optics, 0.38 nm resolution) via an optical fiber for the spectral analysis. A large area silicon detector (Thorlabs DET100A) is used to calibrate the emission collection system, where the detector is placed directly on the emitting ring with the collected power as the reference. Next, the power is compared to the photon counts from the spectrometer for the calibration. A TEC is used to control the on-chip temperature T of MRR device in the various stages of the experiment.

Results

Determination of linear and nonlinear TO coefficient ratios $\tau_{\rm t}$

By using the experimental setup shown in Fig. 2(d), the response of the TH mode emission at various temperatures T are obtained by scanning the pump signal across the free spectral range (FSR) of the MRR while maintaining the device temperature constant with the TEC[12]. The measured wavelength of maximum TH emission at various T of the different TM TH modes at two adjacent resonances of the MRR near 1550 nm is shown in Fig. 3(a). Fig. 3(b) shows the measured maximum intensities of the TH modes of Fig. 3(a) as a function of $I_{\rm p}$. The result shows that it is feasible to classify these modes according to their THG efficiencies, with values in the order of 1.0 nJ^{-2}, 0.05 nJ^{-2}, 0.001 nJ^{-2}, as type I, type II, and type III, respectively. Here, we calculated the THG efficiencies of type I TH modes by using $I_{\rm tmax}^{'}=\mathcal{R}I_{\rm tmax}=4\mathcal{R}g_{\rm TH}^2I_{\rm pmax}^3\big/(3\kappa_t^2)=\mathcal{R}\eta\, I_{\rm pmax}^3$, with η as the THG efficiency. Since we can only measure the scattered signal of the TH emission instead of directly measuring the intra-cavity TH emission energy, η cannot be fully determined due to the unknown overall photodiode responsivity of the collimator $\mathcal{R}$. The measured THG efficiencies $\mathcal{R}\eta$ are 0.937 nJ^{-2} in R-1 and 0.454 nJ^{-2} in R-2.

Besides the THG efficiencies, each type has its own unique values of $\xi_{\rm t}$ and $\Theta_{\rm t}$ that can be extracted from the effective TDWS measurement at two or more resonance locations of the modes. The calculated $\xi_{\rm t}$ and $\Theta_{\rm t}$ of the type I and type II TH modes in table 1 show that the linear TO coefficient $\xi_{\rm t}$ of these TH modes have similar values as the pump mode $\xi_{\rm p}$ where all four TM-TM THG cases having negative thermal matchings, with $\Delta\tau<0$. This is caused by their linear TO phase mismatches over-equalizing the nonlinear TO phase mismatches. For these TH modes, their TDWS rates $d_{\rm t}$ are proportional to the thermal mismatch $-\Delta\tau$.

Demonstration of configurable TDWS and athermal THG in MRRs

For HDSG MRRs, the measured nonlinear TO shift rate $\Theta_{\rm p}$ of the TM pump mode decreases more rapidly than the TE mode across the C- and L-bands, (see Supplementary Fig. S2(b). The result indicates different polarization combinations of the pump mode and the generated TH mode give rise to $\Delta\tau$ with different signs, which can lead to a positive, negative, or even zero TDWS. In MRRs R-1 and R-2, with 200–300 mW TM pumps, TE athermal TH modes with TDWS of $|3d_{\rm t}|\le 0.62$ pm/°C can be achieved as shown in Figs. 4(a) and 4(b). Figure 4(c) compares the measured photon count on the peak of

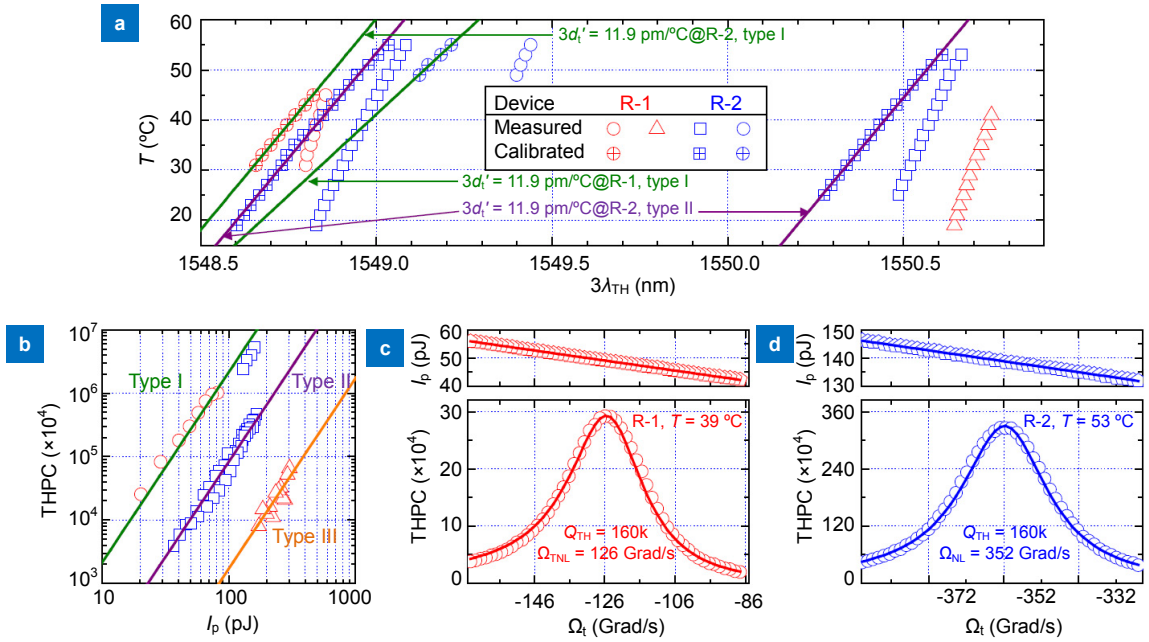

Fig. 3. | (**a**) Measured pump wavelength corresponding to the peak resonances of three types of TM TH modes. The calibrated cold-cavity resonance wavelengths were obtained by subtracted Ω_{TNL} which are shown in plus center symbols. The calibrated TDWS of Type I (green lines) and Type II (purple lines) TH modes are also shown. (**b**) Measured third harmonic photon counts (THPC) on the resonance peaks of the TH modes as a function of I_p showing the cubic TH-pump relationship. The solid lines show the cubic TH-pump relationship for comparison. (**c** – **d**) The measured I_p (upper) and filter response (lower) of corresponding type I TH modes as functions of Ω_t in the devices of R-1 (c) and R-2 (d) respectively. The Q-factor of TH modes Q_{TH} can be indirectly determined by using Θ_t = 2.55×10^9 rad/pJ into Eq. (4). The corresponding fitted curves using estimated Q_{TH} are also shown in (c) – (d). Here, the symbols of the measured data in (b) – (d) are the same as those in (a).

Table 1 | The corresponding parameters of Figs. 3(a) and 3(b). Details of corresponding pump mode parameter measurement are discussed in Supplementary information.

Device	Pump mode				TH mode			TH mode type	Δτ (pJ/ºC)	$3d_t$ (pm/ºC)
	λ_{p0} (nm)	ξ_p (1/ºC)	Θ_p @39 ºC (rad/pJ)	τ_p (pJ/ºC)	ξ_t (1/ºC)	Θ_t (rad/pJ)	τ_t (pJ/ºC)			
R-1	1548.88	1.23×10^{-5}	1.88×10^9	5.19	7.66×10^{-6}	2.55×10^9	6.84	Type I	−1.35	4.2[a]
	1550.28	1.21×10^{-5}	1.21×10^9	7.58	N/A[c]	N/A[c]	N/A[c]	Type III	N/A[c]	5.2[a]
R-2	1549.16	1.29×10^{-5}	1.88×10^9	5.22	9.95×10^{-6}	2.55×10^9	8.89	Type I	−3.67	6.7[b]
					7.71×10^{-6}	2.00×10^9	8.81	Type II	−3.59	7.1[a]/8.4[b]
	1550.73	1.28×10^{-5}	1.80×10^9	5.40	7.69×10^{-6}	2.00×10^9	8.77	Type II	−3.37	6.3[a]/7.9[b]

[a]Fitting data within T = 31 ºC ~ 45 ºC. [b]Fitting data within T = 47 ºC ~ 55 ºC. [c]Values cannot be extracted due to the measured wavelength shift is below the OSA resolution limit.

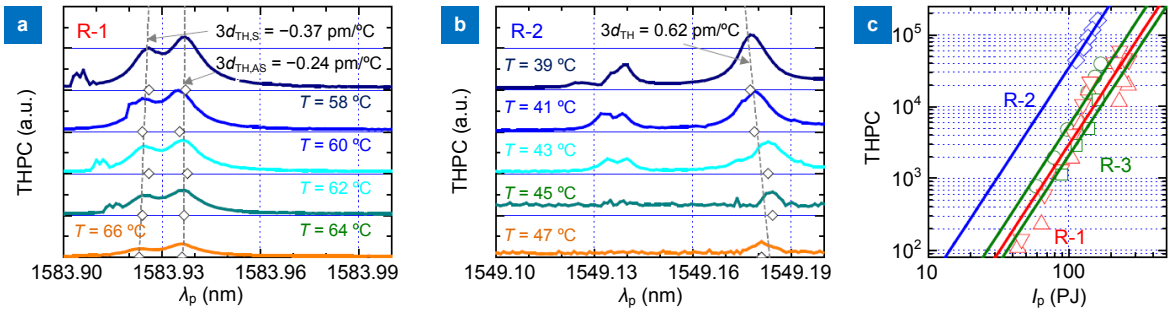

Fig. 4. | (**a – b**) Measured spectra of all the TE athermal TH modes in MRRs of R-1 (a) and R-2 (b) that are thermal matched, i.e. Δτ ≈ 0. In (a) and (b), the measured wavelengths of the resonance peak of TH modes at different T are shown in open diamonds. The corresponding fitted TDWS of TH modes are shown in grey dashed lines. (**c**) The measured photon count on the peak of different athermal TH modes as a function of I_p. The solid lines show the cubic TH-pump relationship for (a) – (b) as well as Figs. 5(c) and 5(e) for comparison. The data and fitting curves for R-1, R-2, R-3 are shown in blue, red, and green, respectively.

TH modes as a function of I_p. As shown in Fig. 4(c), in device R-2 the generated TE athermal TH mode has a THG efficiency of $\mathcal{R}\eta = 0.0226$ nJ^{-2}, which is one order of magnitude smaller than that of type I TM-TM THG combination. We also notice that the measured THG efficiency of the TE athermal modes is proportional to the Q-factor of MRR. The device R-2 with higher Q-factor can achieve THG efficiency one order of magnitude greater than that in R-1.

To verify the results, a second device R-3 is measured, having the same design as R-1. As shown in Fig. 4(c), the two measured TE athermal TH modes in R-3 have similar THG efficiencies as R-1, which indicates that they belong to one TH mode family. The measured spectra of these two athermal TH modes in MRR R-3 generated by TM-TE combination were shown in Fig. 5(c) and Fig.

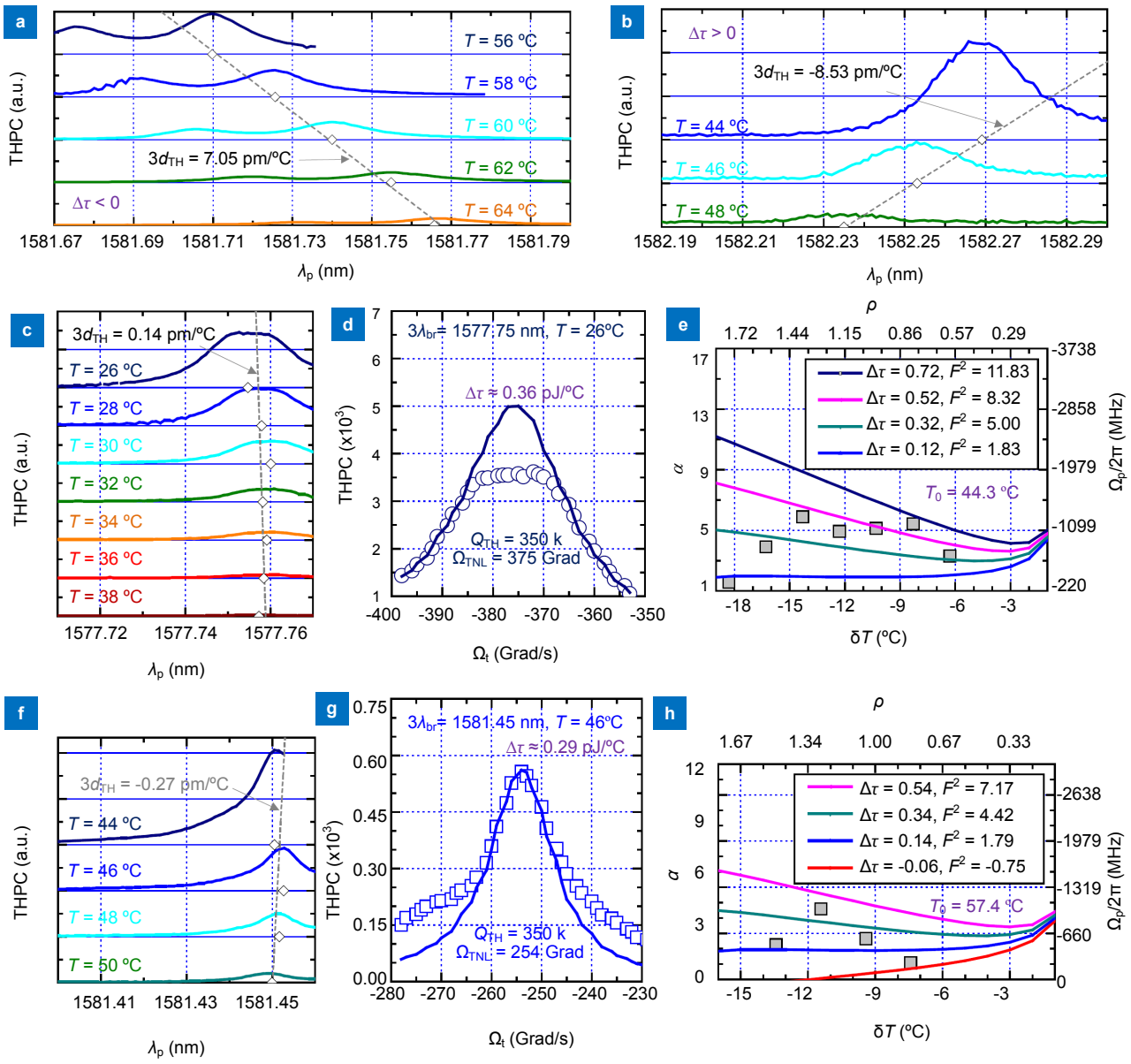

Fig. 5 | (**a**) Thermal mismatch $\Delta\tau < 0$, with a TM pump generated a TM TH mode with a TDWS of $3d_{TH}$ = 7.05 pm/°C. (**b**) Thermal mismatch $\Delta\tau > 0$, with a TE pump generated a TE TH mode with $3d_{TH} = -8.53$ pm/°C. (**c**, **f**) When thermal mismatch $\Delta\tau \approx 0$, with a TM pump generated TE TH mode with $3d_{TH}$ = 0.14 pm/°C (c) as well as $3d_{TH} = -0.27$ pm/°C (f). (**d**, **g**) The extracted Q-factor of TE TH modes by using the data in (c) at 26 °C and in (f) at 46 °C, with Eq. (4) is used to generate the fitted lines. (**e**, **h**) The temperature dependence of the athermal TH mode resonance fluctuation with fixed $\Delta\tau$ and F^2 for the TH modes shown in (c) and (f), with the measured values in gray squares. In (a – c) and (f), the measured wavelengths of the resonance peak of TH modes at different T are shown in open diamonds. The corresponding fitted TDWS of TH modes are shown in grey dashed lines.

5(f). In the same device, Fig. 5(a) shows that, with the TM pump mode, the generated TM TH visible mode yields d_t = 2.35 pm/°C which is close to that of R-2 shown in Table 1. In this case, a negative $\Delta\tau$ leads to a positive TDWS. For the TE-TE combination in Fig. 5(b), it gives rise to a negative TDWS of d_t = −2.84 pm/°C due to the under-compensation of the linear TO effect. The results indicate that the TE-TE and TM-TM combination having opposite TDWS trends. Athermal operation with perfect thermal matching $\Delta\tau \approx 0$ can be achieved with the TM-TE combination in R-1 (Fig. 4(a)), R-2 (Fig. 4(b)), and R-3 (Figs. 5(c) and 5(f)). Figure 5(c) show an TDWS at the TH wavelength of only $|d_t| \le 0.09$ pm/°C can be achieved in R-3, which is a clear demostration of the use of linear TO phase mismatch to equalize the nonlinear TO phase mismatch when thermal matching occurs. This also shows that by selecting different combinations of the pump and TH modes, one can control the direction of the TDWS via configuring the thermal mismatch $\Delta\tau$ in these HDSG MRRs.

For athermal TH modes, since the measured pump wavelength slope is less than the resolution of the OSA of 1 pm, it is not possible to calculate ξ_t and Θ_t accurately as in Fig. 3(a). From Eq. (2), the nearly phase matching assumption of the athermal modes can be used to determine the pump detuning Ω_p and T_0. Figures 5(c) and 5(f) indicates the two TE TH modes belong to the same type of TH mode in MRR R-3 and have similar ξ_t in the L-band. By assuming that the ratio of ξ_t to Θ_t in R-3 is the same as that in R-1 as shown in table 1, we get a trial value of $\xi_t = 9.0\times10^{-6}$ /°C. From the data of Figs. 5(c) and 5(f), we can obtain $\Delta\tau$ = 0.36 pJ/°C and $\Theta_t = 2.3\times10^9$ rad/pJ for Fig. 5(c) and $\Delta\tau$ = 0.29 pJ/°C and $\Theta_t = 1.9\times10^9$ rad/pJ for Fig. 5(f) by using the estimated ξ_t.

One can also estimate Q_{TH} of the TE TH mode by using the extracted Θ_t and ξ_t along with the assumption of $\Delta\tau \approx 0$. Figs. 5(d) and 5(g) show the measured spectrum and fitted curve using Eq. (4) and the estimated values of $\Delta\tau$ and Θ_t. As shown in Figs. 5(d) and 5(g), both of the athermal TH modes have a Q_{TH} of 3.5×10^5, which is close to the intrinsic Q of the TH mode and smaller than $Q_p = 4.32\times10^5$ of the pump mode.

Discussion

For the HDSG MRR, the measured Θ_p is approximately two orders of magnitude higher than the shift rate from the Kerr effect. Such difference is about 10 times greater than that in the Si_3N_4 MRR[17]. Meanwhile, both of these platforms have similar linear TDWS at around 20 pm/°C[13–18]. It indicates that in the HDSG MRRs, the nonlinear TO effect can redshift the resonance of pump mode over a much broader bandwidth of about 10 times compared to the Si_3N_4 MRR. This covers more TH mode resonances and makes thermal matching easier to be achieved by finding a close to zero $\Delta\tau$ in the HDSG MRRs. We notice that MRRs with different gap separations between the bus and ring, coupling rates, and Q-factors, also lead to different wavelength dependent values of Θ_p[17].

The model in Eq. (5) also provides insights to maximize the Θ_p value for broadening the temperature range of stable atheraml THG. Since the real roots of α in Eq. (5) only exist when $|F^2| \ge |\rho|$ and the smaller roots cannot lead to an athermal mode, from $\alpha = \rho \pm \sqrt{F^2/\rho - 1}$, we have

$$\Omega_p = \Theta_p \Delta\tau |\delta T| + \sqrt{\frac{\kappa_{pe} P_i}{\tau_t |\delta T|} - \frac{\kappa_p^2}{4}} \quad . \tag{6}$$

Equation (6) determines the dependence of athermal TH resonance frequency on temperature fluctuation δT, in which the first and second terms on the right-hand side of Eq. (6) represents the linear TO effect and the

Table 2 | Comparison of athermal TDWS schemes using different micro resonators.

Ref.	Temp. range (°C)	Effects to compensate	Compensation method	TDWS (pm/°C)	Gain	Polarization	Material
Ref.[33]	9~25	Linear TO	Polymer cladding	0.2	No	TE	SOI
Ref.[35]	25–90	Linear TO	sol-gel cladding	0.9	No	TM	SOI
Ref.[37]	22–28	Linear TO	a-TiO2 cladding	−1.6	No	-	Si
Ref.[40]	-	Nonlinear TO	w etched Si slab	N/A	No	TE	Si
This work	26–38	Linear TO & nonlinear TO	Thermal matching	0.05	Yes	TE(TH) TM(pump)	HDSG

nonlinear TO effect, respectively. The increase of $|\delta T|$ can simultaneously enhance the first term and reduce the second, and vice versa, which gives a similar form as the bandgap reference in electrical circuit design[49]. With a non-zero and positive $\Delta\tau$, the linear TO effect can equalizes the nonlinear TO effect over a certain temperature range and provide temperature independent frequency reference when the pump frequency is fixed. In contrast to the external linear feedback control scheme[17,42], the thermal matching can automatically retain the phase matching of THG in the athermal mode.

Equation (6) also shows the operating temperature range of athermal THG can be determined by setting the calculated $\partial\Omega_p/\partial(\delta T)$ to zero, which gives an approximately inversed cubic relationship between δT and τ_t. Since the values of ξ_t are on the same order of ξ_p, a close to zero τ_t can easily be obtained with a large Θ_p value, which is in the same order as Θ_t for broadening the operating temperature range. Contrarily, although the athermal THG still exists at small Θ_p values, it shrinks the operating temperature range to less than one degree and severely limits its effectiveness.

Using the parameters extracted from the measured athermal TH modes, the calculated α as functions of ρ at a fixed $\Delta\tau$ are plotted in Figs. 5(e) and 5(h) using Eq. (5). The gray squares in Figs. 5(e) and 5(h) are from the measured result of Figs. 5(c) and 5(f), respectively. It shows a non-zero and positive $\Delta\tau$ (0.3 pJ/°C) can achieve perfect power insensitive athermal THG with less than hundreds of MHz variation within 12 °C and 6 °C ranges, respectively. This range is comparable to the reported passive athermal TDWS approaches for MRRs[34,38] as shown in table 2. In Figs. 5(e) and 5(h), note that the variation of their wavelengths is only a few picometers, which is close to the accuracy limit of TLS and OSA.

Conclusions

In conclusion, we present a comprehensive study of the thermal behavior of the visible modes in micro-resonators generated by the THG process pumped with telecom wavelengths. A dynamic model that includes both the linear and nonlinear TO effects is used to explain the pump and third harmonic resonance shifts for a given input pump power in the MRRs. Using this model, we predict and experimentally demonstrate visible third harmonics modes having TDWS between −2.84 pm/°C and 2.35 pm/°C when pumped at the L-band. By precisely matching the pump and the TH modes at different thermal mismatches, it is now possible to configure effective TDWS for a given MRR leading to athermal THG at different wavelengths. We have also identified orthogonally pumped athermal visible TH modes with a TDWS of 0.05 pm/°C over a temperature range of 12 °C. In table 2, we compared the proposed deterministic athermal THG scheme with other athermal approaches which use a negative TO coefficient overlay to compensate linear TO effect or equalize the nonlinear TO effect by optimizing the structure of MRRs. Unlike the previous works, our proposed scheme uses only one CW laser pump with fixed wavelength and power to directly generate athermal TH modes in a silicon rich CMOS-compatible MRRs without any external compensation scheme. This configurable THG approach can generate athermal visible emission mode with high Q-factor, approximately-zero TDWS, tens of degree temperature range, and no operation bandwidth limitation. This finding further promises the realization of temperature insensitive highly efficient THG for potential $2f$–$3f$ self-referencing in metrology, biological and chemical sensing applications.

References

1. Carmon T, Vahala K J. Visible continuous emission from a silica microphotonic device by third-harmonic generation. *Nat Phys* **3**, 430–435 (2007).
2. Corcoran B, Monat C, Grillet C, Moss D J, Eggleton B J et al. Green light emission in silicon through slow-light enhanced third-harmonic generation in photonic-crystal waveguides. *Nat Photonics* **3**, 206–210 (2009).
3. Sasagawa K, Tsuchiya M. Highly efficient third harmonic generation in a periodically poled MgO: $LiNbO_3$ disk resonator. *Appl Phys Express* **2**, 122401 (2009).
4. Farnesi D, Barucci A, Righini G C, Berneschi S, Soria S et al. Optical frequency conversion in silica-whispering-gallery-mode microspherical resonators. *Phys Rev Lett* **112**, 093901 (2014).
5. Asano M, Komori S, Ikuta R, Imoto N, Özdemir Ş K et al. Visible light emission from a silica microbottle resonator by second- and third-harmonic generation. *Opt Lett* **41**, 5793–5796 (2016).
6. Liu H L, Zhang Z B, Shang Z C, Gao T, Wu X J. Dynamically manipulating third-harmonic generation of phase change material with gap-Plasmon resonators. *Opt Lett* **44**, 5053–5056 (2019).
7. Levy J S, Foster M A, Gaeta A L, Lipson M. Harmonic generation in silicon nitride ring resonators. *Opt Express* **19**, 11415–11421 (2011).
8. Wang L R, Chang L, Volet N, Pfeiffer M H P, Zervas M et al. Frequency comb generation in the green using silicon nitride microresonators. *Laser Photonics Rev* **10**, 631–638 (2016).
9. Lu X Y, Moille G, Li Q, Westly D A, Singh A et al. Efficient telecom-to-visible spectral translation through ultralow power nonlinear nanophotonics. *Nat Photonics* **13**, 593–601 (2019).
10. Surya J B, Guo X, Zou C L, Tang H X. Efficient third-harmonic generation in composite aluminum nitride/silicon nitride

microrings. *Optica* **5**, 103–108 (2018).
11. Guo X, Zou C L, Jiang L, Tang H X. All-optical control of linear and nonlinear energy transfer via the Zeno effect. *Phys Rev Lett* **120**, 203902 (2018).
12. Lin J T, Yao N, Hao Z Z, Zhang J H, Mao W B et al. Broadband quasi-phase-matched harmonic generation in an on-chip monocrystalline lithium niobate microdisk resonator. *Phys Rev Lett* **122**, 173903 (2019).
13. Li Y H, Wang S H, Tian Y Y, Ho W L, Li Y Y et al. Third-harmonic generation in CMOS-compatible highly doped silica micro-ring resonator. *Opt Express* **28**, 641–651 (2020).
14. Rodriguez A, Soljačić M, Joannopoulos J D, JohnsonS G. $\chi^{(2)}$ and $\chi^{(3)}$ harmonic generation at a critical power in inhomogeneous doubly resonant cavities. *Opt Express* **15**, 7303–7318 (2007).
15. Zhang X Y, Cao Q T, Wang Z, Liu Y X, Qiu C W et al. Symmetry-breaking-induced nonlinear optics at a microcavity surface. *Nat Photonics* **13**, 21–24 (2019).
16. Liu B D, Yu H K, Li Z Y, Tong L M. Phase-matched second-harmonic generation in coupled nonlinear optical waveguides. *J Opt Soc Am B* **36**, 2650–2658 (2019).
17. Guo H, Karpov M, Lucas E, Kordts A, Pfeiffer M H P et al. Universal dynamics and deterministic switching of dissipative Kerr solitons in optical microresonators. *Nat Phys* **13**, 94–102 (2017).
18. Bao C Y, Xuan Y, Jaramillo-Villegas J A, Leaird D E, Qi M H et al. Direct soliton generation in microresonators. *Opt Lett* **42**, 2519–2522 (2017).
19. Xue X X, Xuan Y, Wang C, Wang P H, Liu Y et al. Thermal tuning of Kerr frequency combs in silicon nitride microring resonators. *Opt Express* **24**, 687–698 (2016).
20. Joshi C, Jang J K, Luke K, Ji X C, Miller S A et al. Thermally controlled comb generation and soliton modelocking in microresonators. *Opt Lett* **41**, 2565–2568 (2016).
21. Lee B S, Zhang M, Barbosa F A S, Miller S A, Mohanty A et al. On-chip thermo-optic tuning of suspended microresonators. *Opt Express* **25**, 12109–12120 (2017).
22. Wang W Q, Lu Z Z, Zhang W F, Chu S T, Little B E et al. Robust soliton crystals in a thermally controlled microresonator. *Opt Lett* **43**, 2002–2005 (2018).
23. Wang C, Zhang M, Zhu R R, Hu H, Loncar M. Monolithic photonic circuits for Kerr frequency comb generation, filtering and modulation. *Nat Commun* **10**, 978 (2019).
24. He Y, Yang Q F, Ling J W, Luo R, Liang H X et al. A self-starting bi-chromatic $LiNbO_3$ soliton microcomb. *Optica* **6**, 1138–1144 (2019).
25. Jost J D, Lucas E, Herr T, Lecaplain C, Brasch V et al. All-optical stabilization of a soliton frequency comb in a crystalline microresonator. *Opt Lett* **40**, 4723–4726 (2015).
26. Zhou H, Geng Y, Cui W W, Huang S W, Zhou Q et al. Soliton bursts and deterministic dissipative Kerr soliton generation in auxiliary-assisted microcavities. *Light: Sci Appl* **8**, 50 (2019).
27. Padmaraju K, Bergman K. Resolving the thermal challenges for silicon microring resonator devices. *Nanophotonics* **3**, 269–281 (2014).
28. Carmon T, Yang L, Vahala K J. Dynamical thermal behavior and thermal self-stability of microcavities. *Opt Express* **12**, 4742–4750 (2004).
29. Ikeda K, Saperstein R E, Alic N, Fainman Y. Thermal and Kerr nonlinear properties of plasma-deposited silicon nitride/silicon dioxide waveguides. *Opt Express* **16**, 12987–12994 (2008).
30. Lee J M. Athermal silicon photonics//Pavesi L, Lockwood D J. Silicon Photonics III: Systems and Applications. Berlin Heidelberg: Springer-Verlag, 2016.
31. Kokubun Y, Funato N, Takizawa M. Athermal waveguides for temperature-independent lightwave devices. *IEEE Photonics Technol Lett* **5**, 1297–1300 (1993)
32. Chu S T, Pan W G, Suzuki S, Little B E, Sato S et al. Temperature insensitive vertically coupled microring resonator add/drop filters by means of a polymer overlay. *IEEE Photonics Technol Lett* **11**, 1138–1140 (1999).
33. Teng J, Dumon P, Bogaerts W, Zhang H B, Jian X G et al. Athermal silicon-on-insulator ring resonators by overlaying a polymer cladding on narrowed waveguides. *Opt Express* **17**, 14627–14633 (2009).
34. Milošević M M, Emerson N G, Gardes F Y, Chen X, Adikaari A A D T et al. Athermal waveguides for optical communication wavelengths. *Opt Lett* **36**, 4659–4661 (2011).
35. Raghunathan V, Izuhara T, Michel J, Kimerling L. Stability of polymer-dielectric bi-layers for Athermal silicon photonics. *Opt Express* **20**, 16059–16066 (2012).
36. Namnabat S, Kim K J, Jones A, Himmelhuber R, DeRose C T et al. Athermal silicon optical add-drop multiplexers based on thermo-optic coefficient tuning of sol-gel material. *Opt Express* **25**, 21471–21482 (2017).
37. Guha B, Cardenas J, Lipson M. Athermal silicon microring resonators with titanium oxide cladding. *Opt Express* **21**, 26557–26563 (2013).
38. Djordjevic S S, Shang K P, Guan B B, Cheung S T S, Liao L et al. CMOS-compatible, Athermal silicon ring modulators clad with titanium dioxide. *Opt Express* **21**, 13958–13968 (2013).
39. Ptasinski J, Khoo I C, Fainman Y. Passive temperature stabilization of silicon photonic devices using liquid crystals. *Materials* **7**, 2229–2241 (2014).
40. Guha B, Kyotoku B B C, Lipson M. CMOS-compatible athermal silicon microring resonators. *Opt Express* **18**, 3487–3493 (2010).
41. Luo L W, Wiederhecker G S, Preston K, Lipson M. Power insensitive silicon microring resonators. *Opt Lett* **37**, 590–592 (2012).
42. Grudinin I, Lee H, Chen T, Vahala K. Compensation of thermal nonlinearity effect in optical resonators. *Opt Express* **19**, 7365–7372 (2011).
43. Jin L, Di Lauro L, Pasquazi A, Peccianti M, Moss D J et al. Optical multi-stability in a nonlinear high-order microring resonator filter. *APL Photonics* **5**, 056106 (2020).
44. Chembo Y K, Menyuk C R. Spatiotemporal Lugiato-Lefever formalism for Kerr-comb generation in whispering-gallery-mode resonators. *Phys Rev A* **87**, 053852 (2013).
45. Godey C, Balakireva I V, Coillet A, Chembo Y K. Stability analysis of the spatiotemporal Lugiato-Lefever model for Kerr optical frequency combs in the anomalous and normal dispersion regimes. *Phys Rev A* **89**, 063814 (2014).
46. Little B. A VLSI photonics platform. In *OFC 2003 Optical Fiber Communications Conference*, 444–445 (IEEE, 2003); http://doi.org/10.1109/OFC.2003.315925.
47. Ferrera M, Razzari L, Duchesne D, Morandotti R, Yang Z et al. Low-power continuous-wave nonlinear optics in doped silica glass integrated waveguide structures. *Nat Photonics* **2**, 737–740 (2008).
48. Moss D J, Morandotti R, Gaeta A L, Lipson M. New CMOS-compatible platforms based on silicon nitride and Hydex for nonlinear optics. *Nat Photonics* **7**, 597–607 (2013).
49. Widlar R J. New developments in IC voltage regulators. *IEEE J Solid-State Circuits* **6**, 2–7 (1971).

Acknowledgements

We are grateful for financial supports from the Natural Science Foundation of Fujian Province (Grant No. 2017J01756); National Natural Science Foundation of China (Grant No. R-IND12101, No. 61675231); Strategic Priority Research Program of Chinese Academy of Sciences (Grant No. XDB24030300).

Author contributions

S. H. W. developed the original concept. B. E. L., R. R. D. and X. W. designed and fabricated the integrated devices. Y. L. performed the experiments. Y. L. and S.T.C. contributed to the development of the experiment. S. H. W., S. T. C., and B. E. L. contributed to the writing of the manuscript. L. W. and S. T. C. supervised the research.

Competing interests

The authors declare no competing financial interests

Supplementary information

Supplementary information for this paper is available at https://doi.org/10.29026/oea.2020.200028.